Holographic Interferometry (HI), Infrared Vision and X-Ray Fluorescence (XRF) spectroscopy for the assessment of painted wooden statues: a new integrated approach

**Stefano Sfarra · Clemente Ibarra-Castanedo ·
Stefano Ridolfi · Giorgio Cerichelli · Dario Ambrosini ·
Domenica Paoletti · Xavier Maldague**

Abstract Wood has been routinely employed in decorative arts, as well as in sculptures and paintings (support) during the Middle Ages, because of its unique aesthetic virtues. It may safely be assumed that wood, as a material for monumental sculpture, was much more commonly employed in the mediaeval period than existing examples would seem to indicate (Bulletin of the metropolitan Museum of Art, 2013). Wood is easily obtainable; it could be carved and put in place with less difficulty than stone, it is chemically stable when dry, and its surface offers a compatible substrate for paint application. However, the use of wood is not without pitfalls, and requires an understanding of its anisotropic and hygroscopic nature. It is also dimensionally unstable and subject to deterioration by fungi and insects. Moisture-related dimensional changes are certainly among the most challenging problems in painting conservation. With the purpose of preventing important damages, the use of non-or microdestructive testing (NDT) techniques is undoubtedly of paramount interest for painted wooden statues of great value. This work has a threefold purpose: (1) to validate the effectiveness of an integrated approach using near-infrared (NIR) reflectography, square pulse thermography (SPT), and holographic interferometry (HI) techniques for discovering old repairs and/or inclusions of foreign materials in a wooden structure, (2) to confirm and approximately date the restoration carried out by x-ray fluorescence (XRF) spectroscopy and energy-dispersive x-ray spectroscopy (EDS) (that is assembled with a scanning electron microscopy—SEM) techniques, and (3) to combine into a multidisciplinary approach two quantitative NDT results coming from optical and thermographic methods. The subject of the present study was a statue named "Virgin with her Child" (XIV century), whose origins are mysterious and not properly documented.

S. Sfarra (✉) · D. Ambrosini · D. Paoletti
Department of Industrial and Information Engineering and Economics, Las.E.R. Laboratory, University of L'Aquila, Piazzale E. Pontieri 1, Loc. Monteluco di Roio, AQ, 67100, Italy
e-mail: stefano.sfarra@univaq.it
Fax: +39-0862-431233

D. Ambrosini
e-mail: dario.ambrosini@univaq.it

D. Paoletti
e-mail: domenica.paoletti@univaq.it

C. Ibarra-Castanedo · X. Maldague
Computer Vision and Systems Laboratory, Department of Electrical and Computer Engineering, Laval University, 1065, av. de la Médecine, Quebec City, G1V 0A6, Canada

C. Ibarra-Castanedo
e-mail: IbarraC@gel.ulaval.ca

X. Maldague
e-mail: Maldagx@gel.ulaval.ca

S. Ridolfi
Ars Mensurae, Via Comparini 101, Rome, 00188, Italy
e-mail: stefano@arsmensurae.it

G. Cerichelli
Department of Physical and Chemical Sciences, University of L'Aquila, Via Vetoio (Coppito 1), Loc. Coppito, AQ, 67100, Italy
e-mail: giorgio.cerichelli@univaq.it

1 Introduction

Depending on the nature of the material being investigated, a suite of techniques may be utilized to assess its structure and properties. Whereas some techniques are qualitative, such as providing an image of a surface, others yield quantitative information such as the relative concentrations of atoms that comprise the material. It should be noted that the sensitivity
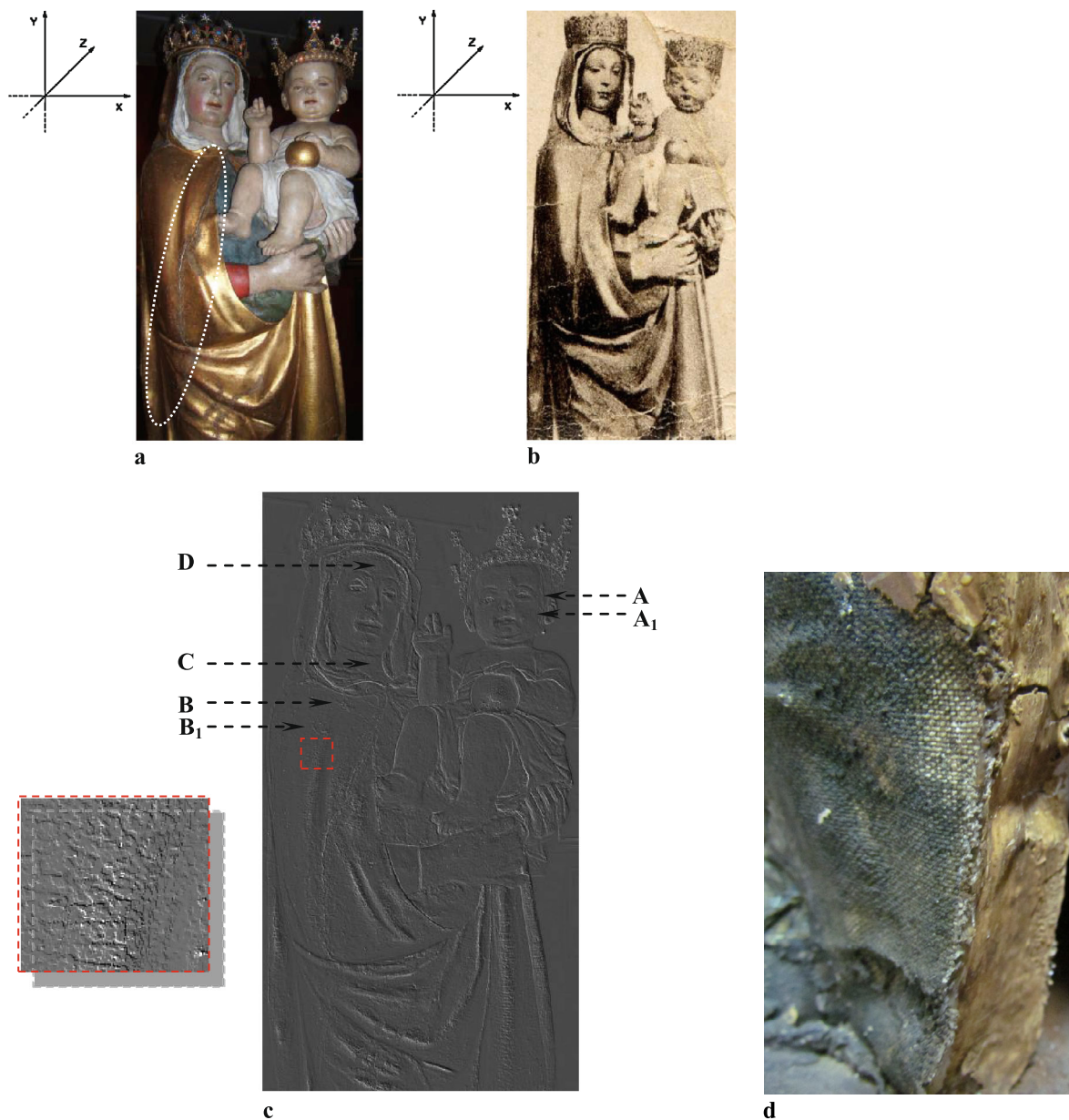
Fig. 1 *Virgin with her Child* statue (XIV century): (**a**) actual state; (**b**) ancient state; (**c**) position of the defects and magnification of a *craquelure* area (emboss effect); and (**d**) traces of the *incamottatura* layer

of quantitative techniques continues to be improved, with techniques now being able to easily measure parts per trillion (ppt) concentrations of impurities in a bulk sample [2].

In the materials characterization field, the main problem of a quantitative analysis for real large-sized objects is the high cost of investing in order to detect the whole structure. Furthermore, in many cases, a quasi-quantitative characterization requires a microdestructive inspection, which is often difficult or even not possible nor desirable to perform in the cultural heritage field due to the number of permissions to be requested in advance and the potential damage that can be produced to such important objects.

In this work, an integration between nondestructive [3, 4] and microdestructive [5] techniques was performed, which can be considered as an innovative approach owing to the original combination of methods, as well as for the object under examination, i.e., a painted structure in cedar wood restored long time ago [6], named the Virgin with her Child (XIV century). Unfortunately, a map of the repairs is not currently available; the only records on hand, are: (a) a historical photograph that has been passed down over time, and (b) some information inherent the fabrication of the statue retrieved from the reading documents later described. Comparing the present condition (Fig. 1a) to the ancient state

(Fig. 1b) of the object under investigation, it is strikingly clear that it has been seriously amended over the years. In particular, the head of the Child seems rotated with respect to the $x-y$ plane, and tilted with respect to the z axis.

The integration of near-infrared (NIR) reflectography [7], square pulse thermography (SPT) [8], holographic contouring [9], and sandwich holography (SH) [10] techniques have been used for the nondestructive testing (NDT) of the wooden statue. An unusual fringes pattern appeared over the area covered by the nose, mouth, and chin of the Child. An abnormal spot was detected over the same area after thermographic data processing as well. Microsamples were then taken from two selected points to be inspected by x-ray fluorescence (XRF) spectroscopy and SEM-EDS analysis [11]. The microsamples were chosen taking into consideration the restorations performed on this part of the statue.

Another purpose of the proposed methodology is the detection of subsurface defects at different depths and of different typology (cracks, detached areas, inclusions of foreign materials), to verify the limits of the NDT techniques relatively to the analyzed materials, and integrating into a multidisciplinary approach two quantitative NDT results inherent defect B (detached area); see Fig. 1c just to understand the positions of each defect. This work explores the possibility of using the holographic contouring and thermographic methods linked to a digital image processing system [12], recently developed in engineering applications for metrology and three-dimensional surface control [13], in order to determine the position, the shape, and the volume of defect B, which was chosen as a reference to analyze the combined approach.

2 Description of the *Virgin with her Child* statue

Even though the statue is currently located in the *Santa Maria della Croce di Roio* Church (L'Aquila, Italy), the style does not appear to be compatible with the classical "abruzzese art." Instead, it is believed that it was rather conceived in the Puglia region, southeast of the Abruzzo region. The structure was accomplished using cedar wood, probably Atlas cedar (C. Atlantica) [6]. Cedar wood is light, soft, resinous, and durable, even when in contact with soil or moisture [14].

Despite the controversy about the mysterious origins of the statue, the *Maria's Zodiac* work, published in Naples in 1715 [15], explains that it was found, according to a popular belief, by monk *Serafino of Montorio*.

In the case of a polychromatic wooden structure, the block of wood has a structural function for the final artwork [16]. The fabrication of a wooden sculpture requires a number of operations related to the characteristics of the material being used. In fact, the small dimensions of the logs used to fabricate the statue have often imposed to proceed by assembling multiple separate pieces using joints and grouting difficult to hide. In addition, the wood nature with the grains, the knots, and the variations in tone and color within parts of wood, would interfere with the final representation of the artwork if the sculpture had not been painted. No surface treatment could hide the structure of the wood, with parallel fiber bundles. Therefore, it is well established that the coating of a polychrome wooden statue was a fundamental part of the artwork during the Middle Ages.

The color, the surface effects of the backgrounds, and the preparation layers, have supported the perception of a whole series of aesthetic and sensory parameters that the wooden material could suggest with more difficulties, particularly in relation to the quality of the carving. The paint film that covered a wooden sculpture was usually uniform, less vibrating in the luministic sense, as the lights and the shadows were generated by modeling the wood; however, in some cases, the molded base could also be depicted by particular paintings. The surface of the represented materials could be more striking (fabrics, brocades, hair), due to the relief treatment of the preparation (smooth, machined, stamped, engraved) stretched over the carved wood. The practice of shaping the body of the statue from a single piece of wood is well attested in the medieval period, as described by the rules of the guild of carvers [17, 18]. The choice of the type of wood was mostly entrusted to the artisan; in general, not seasoned logs or emptied insides from the back side were used in order to avoid cracking, which due to the difference between the withdrawal tangential and the radial one, occurs during the maturing process on the whole logs. The presence of the large cavity on the back side of the Virgin with her Child statue is most likely attributable to this kind of practice.

The assembly of the various pieces was performed by means of joints fixed with animal glues, with pegs of wood, or with metal pins, generally of iron, which often are the cause of the cracks inside the wood, due to the increase in size of the corroded metal. The wooden statues, once the phase of the carving has been completed, were covered by a polychrome coating applied over a *preparation* layer. The *preparation* is the set of intermediate layers that lies between the wooden support and the paint film or gilding, and that served to provide a surface physically and chromatically adapted to be painted or to be finished with a gold leaf. It also provided a bond between the support and the pictorial material, in such a way that the latter could follow the movements of the timber without growth of defects. In the preparation layer, a mixture of chalk and animal glue has been spread on a canvas and then the composite material obtained was directly applied to the surface already carved. This process is named *incamottatura*. It had the function of a buffer layer between wood and plaster, as well as it is able to cushion the natural movements of the support. As said, the

incamottatura was then coated by plaster, which undergone different final treatments, connoting the surfaces with special features, using thin and uniform cuts, to dull or roughen the appearance of certain areas or to create drawings and decorations in relief. The practice of applying the plaster layer above the *incamottatura* layer is well documented in [19]. Traces of this layer can be seen in Fig. 1d that represents a part of the blue dress of the Virgin (lowest part).

The visual and sensory surfaces plastically modeled correspond to a significant color change: In the case of the Virgin with her Child, faces and hands are painted, while the clothes and the robe of the Virgin are gilded and painted. The gilding was carried out by applying gold foil on the red *bolus*. This technique is traditionally used since ancient times; it provides the spread of a metal layer with a mixture of water and glue or white egg spread on a layer of clay of red color, called *bolus*. Often during the finishing phase, the gold leaf was burnished with an agate stone, in order to make shiny the surfaces that were smooth and not worked.

The description of stratigraphy and the composition of materials that constitute the statue have been extrapolated from very old books, personal communications, or ancient manuscripts passed down over the years and written by reliable authors [20–25].

In the cultural heritage field, the deterioration of the materials is a natural process and is unstoppable due to intrinsic factors of the work itself, related to the type of material or the type of work, and the environment in which it was preserved. In fact, one of the factors that affects the conservation of a wooden artifact is the environment in which it was preserved, because of the relative humidity (U.R. %) variations or temperature changes (T_{amb} °C) that give rise to numerous degenerative phenomena of the material, such as deformations of the wood (swelling and shrinkage processes), damages, cracks, and dissemination of microbiological attacks. Since the conditions in which the Virgin with her Child statue was preserved over the centuries are unknown, it was not possible to assess how the environmental parameters may have affected the degradation phenomena. The reactions related to changes in the relative humidity, and the consequent dimensional changes of the wood during the expansion and contraction processes, are linked to the large damage of the Virgin's dress (Fig. 1a—dotted oval) which, starting from the base of the neck, goes down vertically through the whole statue.

3 Nondestructive and microdestructive testing techniques used

3.1 Holographic Interferometry (HI)–Sandwich Holography (SH)

Holographic interferometry (HI) is a well-known tool in NDT [26]. The basic goal of HI is the comparison of an object of interest with itself under different operating conditions. Sandwich holography (SH) or, more precisely sandwich HI, is a particular ingenious form of holographic interferometry based on the concept of recording two exposures on different plates. This technique gives more versatility to the double exposure set up; instead of making a double-exposure on one holographic plate, the two exposures are made on different plates, which are then combined in a plate holder. The image, reconstructed from a sandwich hologram gives the same fringes of a conventional double-exposure hologram but, by having the images on two different plates; it is possible to combine them, by shifting and tilting, in order to display the analysis.

3.1.1 Sandwich holographic contouring

Holographic contouring is a simple and flexible method of producing a contour map of the shape of a three-dimensional object with a contour interval from 1 to 300 μm; this image provides an easily interpreted map of the surface shapes, well suited for automatic processing. There are several ways to generate contour maps [27–31]. In this work, it is reported the result obtained with an experimental arrangement based on the sandwich holography technique [10], i.e., by incorporating a minimal displacement of the point of illumination between the exposures. The reconstructed interferograms are captured in real time by a charge-coupled device (CCD) video camera; the video signal is received by a digital card and can be displayed on a monitor or stored for further analysis. Then the stored image is automatically processed by a proper software, which provides the quantitative value of the defect under analysis.

The principle of sandwich holographic contouring, originally devised by Abramson [31], is based on two exposures made on separate plates. Each position of the illuminating source is linked to an exposure. Then the holograms are simultaneously reconstructed combining the two plates in an adjustable plate holder. The two plates can be moved independently, allowing to remove small-rigid-body displacements. For a more in-depth explanation, interested readers can consult [10]. The experimental setup used herein is schematized in Fig. 2.

The processing sequence of the fringes pattern was as follows: A charge-coupled device (CCD) video camera, supported by an image's digitizer with C language software was used to read the photographic contoured image, or directly, the holographic image. Starting from the hypothesis that the first few lines were not distorted, a procedure of correlation was used. Setting conditions and data were written into an ASCII file. The fringes pattern was transformed into a line pattern using a correlation procedure. For each line, an autocorrelation algorithm was used in order to find the period of the fringes expressed in pixel units. If I and J represent

Fig. 2 Sandwich holographic contouring experimental setup
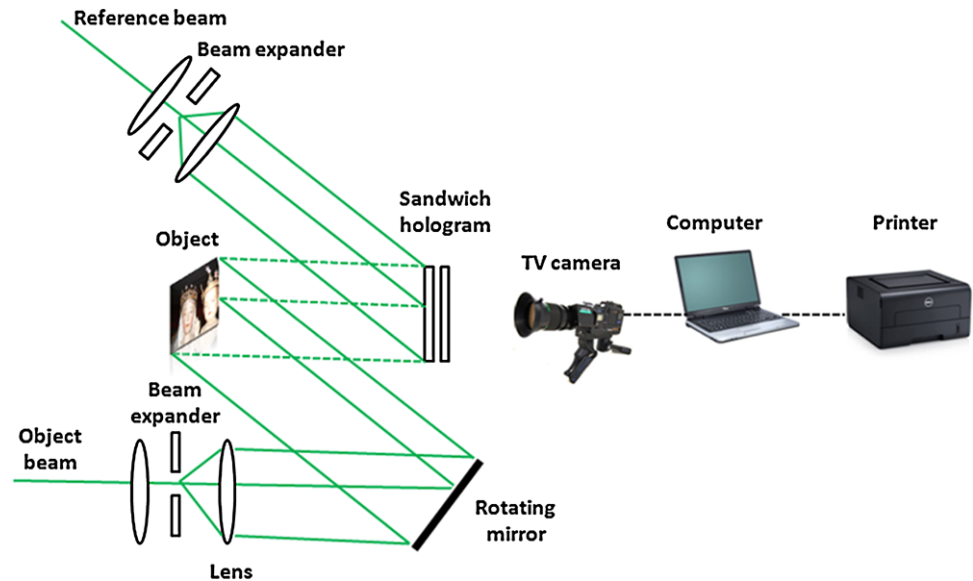
the coordinates of the frame and the lines are oriented along the J coordinate, the autocorrelation method was defined as

$$A_k = \sum_{J=150}^{350} X(I, J)X(I, J + k) \qquad (1)$$

The maximum of the autocorrelation (function of k) was obtained if at least five autocorrelations, corresponding to the shift of 1 pixel, were positioned on a parabola and their difference was greater than a fixed threshold. The T period (i.e., the k_{max}) was calculated with a precision of a fraction of a pixel (≈ 0.2 pixel). Subsequently, using a correlation function between the system of the fringes and a step function, the minima and the maxima of the fringes were detected. This procedure, used for the I coordinates, allows the computing of the fringes' profile. The defect was measured analyzing the distortion of the obtained lines pattern. Collimated illumination could be required if the contour interval remains constant through the depth of the object, although this has not prevented the successful of the use of divergent light in the present system. In addition, the system provides the automatic discrimination of the concavity or convexity of the pattern of the contours.

3.2 X-ray fluorescence (XRF) spectroscopy

XRF is a method for the qualitative and quantitative analysis of chemical elements. It is in principle applicable to all elements of the periodic system with the exception of the first two: hydrogen (H) and helium (He), thereby covering an energy region from about 50 eV to 100 keV [32].

In XRF analysis, a source of x-rays irradiates a sample. The source can be an x-ray tube or a sealed radioisotope. When a sample is irradiated with x-rays, the source x-rays may undergo either scattering or absorption by the sample atoms. When an atom absorbs the source x-rays, the incident radiation can dislodge electrons from the innermost shells of the atom, creating vacancies. Electrons from outer shells will fill the inner shell vacancy and emit x-ray photons. The energy of the emitted x-ray depends on the difference in energy of the shell with the initial vacancy and the energy of the electron that fills the vacancy. Each atom has a specific level, so the emitted radiation is characteristic of that atom. By measuring the energy of the radiation emitted, it is possible to identify which elements are present in a sample. By measuring the intensity of the emitted energies, it is possible to quantify how much of a particular element is present in a sample [33, 34].

In this work, an EDXRF system (energy dispersive) composed of an air-cooled (W-anode) x-ray tube with an active spot of 1.5 mm and working with 35 kV high voltage and 0.2 mA current together with a Peltier cooled SDD (silicon drift detector) was used for the polychromatic painted wooden statue described above [35–37]. The energy resolution was 149 eV at the K_α line of iron.

XRF is usually seen as a nondestructive method, but the exact meaning of this term must be clarified. For the analyst, the specimen is a small piece of material, which may have at least required cutting into shape to fit into a specimen holder, and has possibly undergone also further treatment by cleaning, polishing, coating, etc. If the analytical procedure does not alter such a specimen, it is said to be non-destructive. Nevertheless, the process of taking a specimen from an object may be a destructive step, or much better a microdestructive step if, as in the present case, only two microparts already detached from the cedar support (due to the *craquelure* process—Fig. 1c), were removed [38]. This procedure

is acceptable from the view point of an art historian or conservator, and suitable for the chemical analysis.

The proposed integrated method seems very pertinent in order to optimize the XRF measurements since the sampling is representative of characteristic parts of a structure, preidentified by means of optical and thermographic techniques.

3.3 Near-infraRed (NIR) reflectography

When exposing an object to a radiation source, e.g., a painting illuminated with a wide-spectrum (from ultraviolet to far infrared—IR) incandescent lamp, part of the radiation will be absorbed by, part will be transmitted through and part will be reflected from the incident surface, depending on the radiation wavelength being observed (Fig. 3). For instance, a visible camera will capture the light (in the visible spectrum 400–700 nm) reflected from the painting surface, providing information about colors and textures.

The near IR (NIR) and short-wave IR (SWIR) parts of the radiation, which contain practically no thermal emissions, can penetrate thin layers of painting before being reflected back to the surface from a nonabsorbing media such as the preparation surface (usually made of chalk and gypsum), while this same radiation will be absorbed by carbon based or other absorbing elements (underdrawings), if present. A NIR/SWIR camera would capture images showing the reflective and absorbing areas trough relatively thin painting layers. For instance, most of the oil paints used for panel painting (usually linseed oil with inorganic suspended oxide or mineral salt pigments [39]) are transparent to NIR/SWIR light, i.e., IR radiation in the near and short-wave IR can pass through thin painting layers containing such pigments; while carbon derivatives (such as graphite and charcoal) are opaque in this spectral regions, i.e., radiation is mostly absorbed by these elements. For instance, brown and gray are more transparent than some light colors, greens and blues are nearly opaque, while most black tones are even more opaque [39].

The transparency in the NIR/SWIR bands is a complex function of: (1) the optical characteristics of the pigment color, (2) the underdrawing material, (3) the paint layer thickness (typically a fraction of millimeter [40]), and (4) the detector wavelength (transparency increases between 1000 and 2500 nm for different configurations [41], generally showing a peak near 2000 nm [42]). A NIR/SWIR camera can be used to reconstruct two-dimensional (2D) images, i.e., *reflectograms*, of the reflected light under the painting layers. Interesting applications include the detection of guiding sketches and signatures (opaque to NIR/SWIR radiation) drawn by the artist prior to the application of painting layers; the detection of hidden paintings (painters often use a previously painted canvas or change their mind during the painting progression), the monitoring of the restoration processes required on aging cultural heritage artworks, and the detection of intentional and unintentional alterations [43–48].
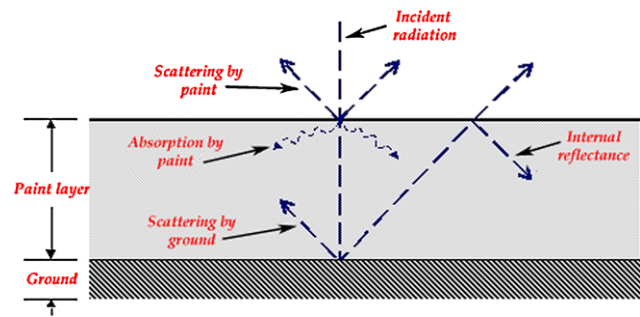

Fig. 3 Interaction of light with paint layer and ground

3.4 Square Pulse Thermography (SPT)

Active thermography is a well-known NDT technique allowing fast inspection of large surfaces that has been extensively investigated [49, 50].

In the square pulse configuration [8, 51], the specimen surface is submitted to a long pulse (from a few seconds to several minutes), and the temperature rise and decay is registered using an infrared camera and stored as a 3D matrix composed by N thermograms, where x and y are the spatial coordinates, and t is the time. Data acquisition is fast and straightforward, as schematized in Fig. 4.

The square pulse function is discontinuous in value and derivative at the beginning and ending points of the pulse. A square pulse is the limit as $n \to \infty$ of:

$$
\begin{aligned}
S_n(x) &= \frac{1}{2} + \frac{2}{\pi} \sum_{k=1}^{n} -1^{k-1} \frac{\cos(2k-1)\omega x}{2k-1} \\
&= \frac{1}{2} + \frac{2}{\pi} \left(\cos \omega x - \frac{1}{3} \cos 3\omega x + \frac{1}{5} \cos 5\omega x + \cdots \right)
\end{aligned}
\tag{2}
$$

where the angular frequency (in radians) is $\omega = 2\pi f$. A plot of this formula for four different values of n is shown in Fig. 5a. Notice that as n increases, the sum of sine functions approximates the form of an ideal square pulse. Generally, a nonperiodic function can also be represented as a sum of sine and cosine functions; otherwise, all frequencies should be used, not just the multiples of the period. This means the sum is replaced by an integral:

$$
f(x) = \frac{1}{2\pi} \int_{-\infty}^{\infty} F(\omega) e^{i\omega x} \, d\omega
\tag{3}
$$

where $e^{i\omega x} = \cos \omega x + i \sin \omega x (i = \sqrt{-1})$. $F(\omega)$ are the coefficients of each sine and cosine; $F(\omega)$ is called the spectrum of the function $f(x)$. The spectrum can be computed from a signal using the Fourier transform. To illustrate the mathematics of the Fourier transform related to the SPT data, the Fourier transform of a square pulse (Fig. 5b) is calculated below. A square pulse is described mathematically

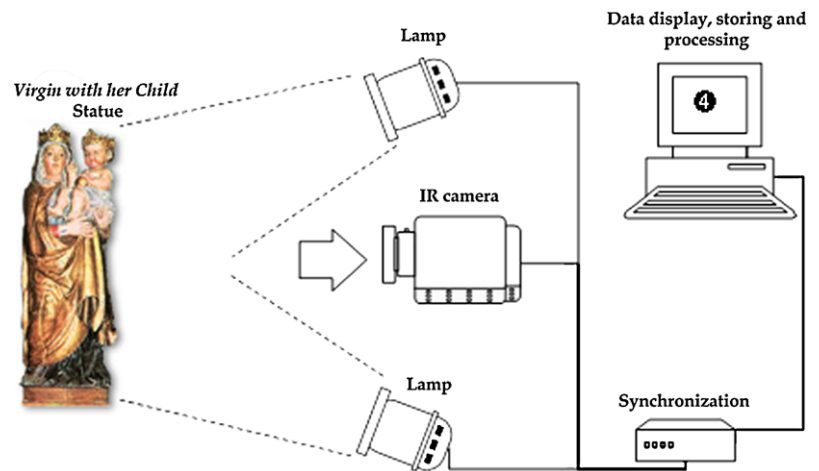**Fig. 5** (**a**) Four approximations to a square pulse. Notice that each approximation involves higher frequency terms and the resulting sum more closely approximates the pulse. As more and more high frequencies are added, the sum converges exactly to the square pulse. Note also the oscillation of the pulse; this is often referred to the Gibbs phenomena, (**b**) the square pulse, and (**c**) the plot of the $\sin c$ function
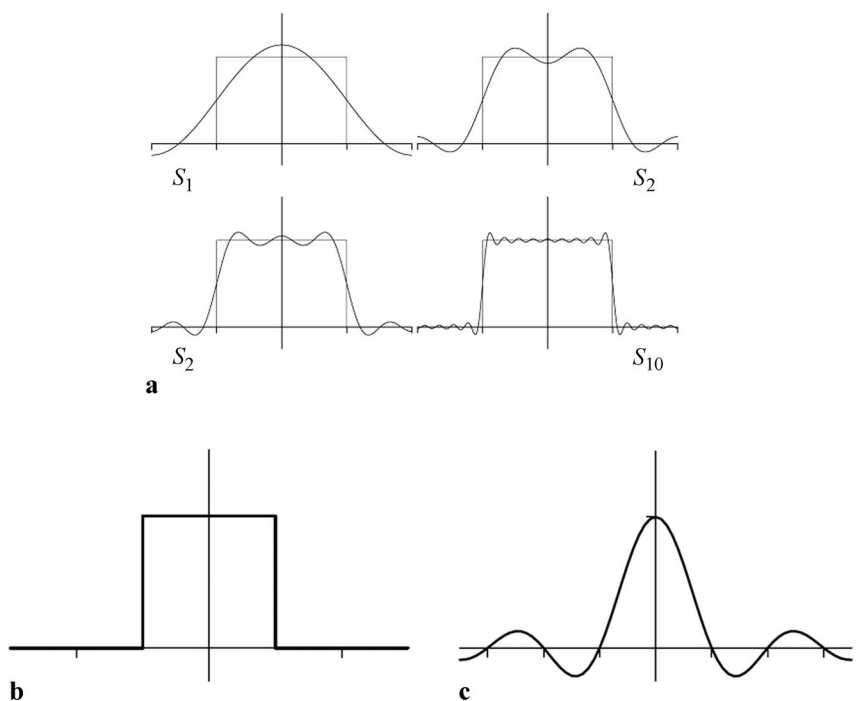
as

$$\text{square}(x) = \begin{cases} 1 \to |x| \leq \frac{1}{2} \\ 0 \to |x| > \frac{1}{2} \end{cases} \tag{4}$$

The Fourier transform of this function is straightforward to compute:

$$\int_{-\infty}^{\infty} \text{square}(x) e^{-i\omega x} \, dx$$

$$= \int_{-\frac{1}{2}}^{\frac{1}{2}} e^{-i\omega x} \, dx = \frac{e^{-i\omega x}}{-i\omega} \bigg|_{-\frac{1}{2}}^{\frac{1}{2}}$$

$$= \frac{e^{i\frac{1}{2}\omega} - e^{-i\frac{1}{2}\omega}}{2i\frac{1}{2}\omega} = \frac{\sin \frac{1}{2}\omega}{\frac{1}{2}\omega} = \sin cf \tag{5}$$

The $\sin c$ function can be defined as

$$\sin cx = \frac{\sin \pi x}{\pi x} \tag{6}$$

Note that $\sin \pi x$ equals zero for all integer values of x, except x equals zero. At zero, the situation is more complicated: Both the numerator and the denominator are zero. However, careful analysis shows that $\sin c0 = 1$, thus

$$\sin c(n) = \begin{cases} 1 \to n = 0 \\ 0 \to n \neq 0 \end{cases} \tag{7}$$

A plot of the $\sin c$ function is shown in Fig. 5c. Notice that the amplitude of the oscillation decreases as x moves from the origin [52].

SPT data is generally processed to improve defect visibility and to performed quantitative characterization of defects. Pulsed phase thermography (PPT) [53, 54], was originally proposed to be applied to pulsed thermography data, for which only the cooling phase is of interest. Nevertheless, it is also possible to use the PPT algorithm with SPT, where both the heating and cooling phases are useful. The latter consideration is also true for the higher order statistics thermography (HOST) technique [55].

In PPT, data is transformed from the time domain to the frequency domain using the 1D discrete Fourier transform (DFT), defined as

$$F_n = \Delta t \sum_{k=0}^{N-1} T(k\Delta t) \exp^{(-j2\pi nk/N)} = \text{Re}_n + j\,\text{Im}_n \quad (8)$$

where j is the imaginary number ($j^2 = -1$), n designates the frequency increment ($n = 0, 1, \ldots, N$), Δt is the sampling interval, and Re and Im are the real and the imaginary parts of the transform, respectively. In this case, real and imaginary parts of the complex transform are used to estimate the amplitude A, and the phase ϕ, as can be seen in Eq. (9):

$$\phi_n = \tan^{-1}\left(\frac{\text{Im}_n}{\text{Re}_n}\right) \quad \text{and} \quad A_n = \sqrt{\text{Re}_n^2 + \text{Im}_n^2} \quad (9)$$

The phase is of particular interest in NDT given that is less affected than raw thermal data by environmental reflections, emissivity variations, nonuniform heating, surface geometry, and orientation. These characteristics are very important in order to strengthen the results discussed in the next section, keeping in mind the colors composition of the statue analyzed, as well as its complex shape and the SPT experimental setup used.

On the other hand, HOST calculates the higher order centralized moments (3rd or *skewness*, 4th or *kurtosis*, or *n*th *order moment*) of the temporal temperature profiles producing single images summarizing all the relevant information about the original sequence [13, 55]. The segmented Kurtogram [56] containing the B defect was compared to the holographic contouring result for metrology purposes.

4 Experimental part: results and discussion

Several types of anomalies were detected after inspecting the "Virgin with her Child" statue (Fig. 1a) by the above reported techniques, such as (see Fig. 1c): splittings (defects B and B_1), cracks (defects C and D), inclusions of foreign materials coming from ancient restorations (defects A and A_1), retouchings in the blue dress of the Virgin, as well as widespread *craquelure*. Figure 1c comes from Fig. 1a, working in the Matlab© environment, and applying the emboss effect explained in depth in the Conclusions section. The intent of this elaboration is to make visible the *craquelure* process, as can be seen in the magnification strictly linked to Fig. 1c. It is not possible to retrieve the shape of the defects by this method, because the original image is a visible image (Fig. 1a). Although they are not noticeable, the points where the defects act are marked by dotted arrows in Fig. 1c just to introduce readers to their position before reading the next paragraphs. The fact that the original image is not blurred and the image processed has a good contrast can be appreciated seeing the magnified part of the Fig. 1c, i.e., the *craquelures'* map. In general, the propagation of the craquelure effect is strictly linked to the paints.

Paints are made by mixing pigments with a liquid binding medium, e.g., drying oil [57, 58]. After applying a layer of paint, it is generally allowed to dry and eventually other layers are added as needed. A final coating of varnish often protects paintings. The thickness for the whole structure ranges from a few micrometers up to 1 mm or more. Varnish and binding media consist of organic compounds, such as vegetable oils, egg yolk, egg white, and resins, and thereby predominantly of light elements, which cause only modest absorption for the fluorescent radiation from the heavier elements. Usually, a pigment is analyzed by its heaviest element, but another selection may be advisable when other pigments containing the same element(s) must be distinguished.

The conditions of measurement inherent to the infrared thermography (IRT) experimental set-ups are described in Table 1 (T: thermo-camera, S: statue, L: lamp(s)). In general, the radiation source consisted of two halogen lamps

Table 1 The main measurement conditions of the IRT set-ups

| Set-up	Defect(s)	Distance between T and S [m]	Distance between L and S [m]	Sampling frequency (f_s) [Hz]	N° of lamps	Heating time [s]	Cooling time [s]	Ambient temperature [°C]	Relative Humidity [%]
1	A and A_1	0.46	0.24	1	2	180	420	26.2	47.5
2	B and B_1	0.56	0.37	1	2	90	300	26.2	47.5
3	B and B_1	0.56	0.50	1	1	10	60	20.1	44.8
4	D	0.61	0.40	1	2	180	420	26.2	47.5
5	C	0.61	0.40	1	2	90	300	26.2	47.5

(OSRAM SICCATHERM—250 W IR), which also provided a wide spectrum radiation (including the NIR band). The lamps were mounted on a linear support. Only for the quantitative characterization of the defect B a halogen lamp (STAR Progetti—2 KW IR) was used. Physical parameters as ambient temperature and relative humidity of the room where the statue was kept were monitored using a De Lorenzo Instruments DLIN TH500 thermo-hygrometer, while in each acquisition a ThermaCam S65 HS by FLIR collected the IRT data.

Comparing the faces of the Virgin and of the Child after (Fig. 1a) and before (Fig. 1b) a restoration, readers can note the modifications in the style of the features. Currently, they appear more rounded.

The NIR inspections, working with a CMOS camera (Canon 40DH 22.2 × 14.8 mm—10 megapixel, spectral

Fig. 6 The Virgin with her Child, NIR results: (**a**) filter VIS, (**b**) filter at 715 nm, (**c**) filter at 850 nm, and (**d**) filter at 1000 nm
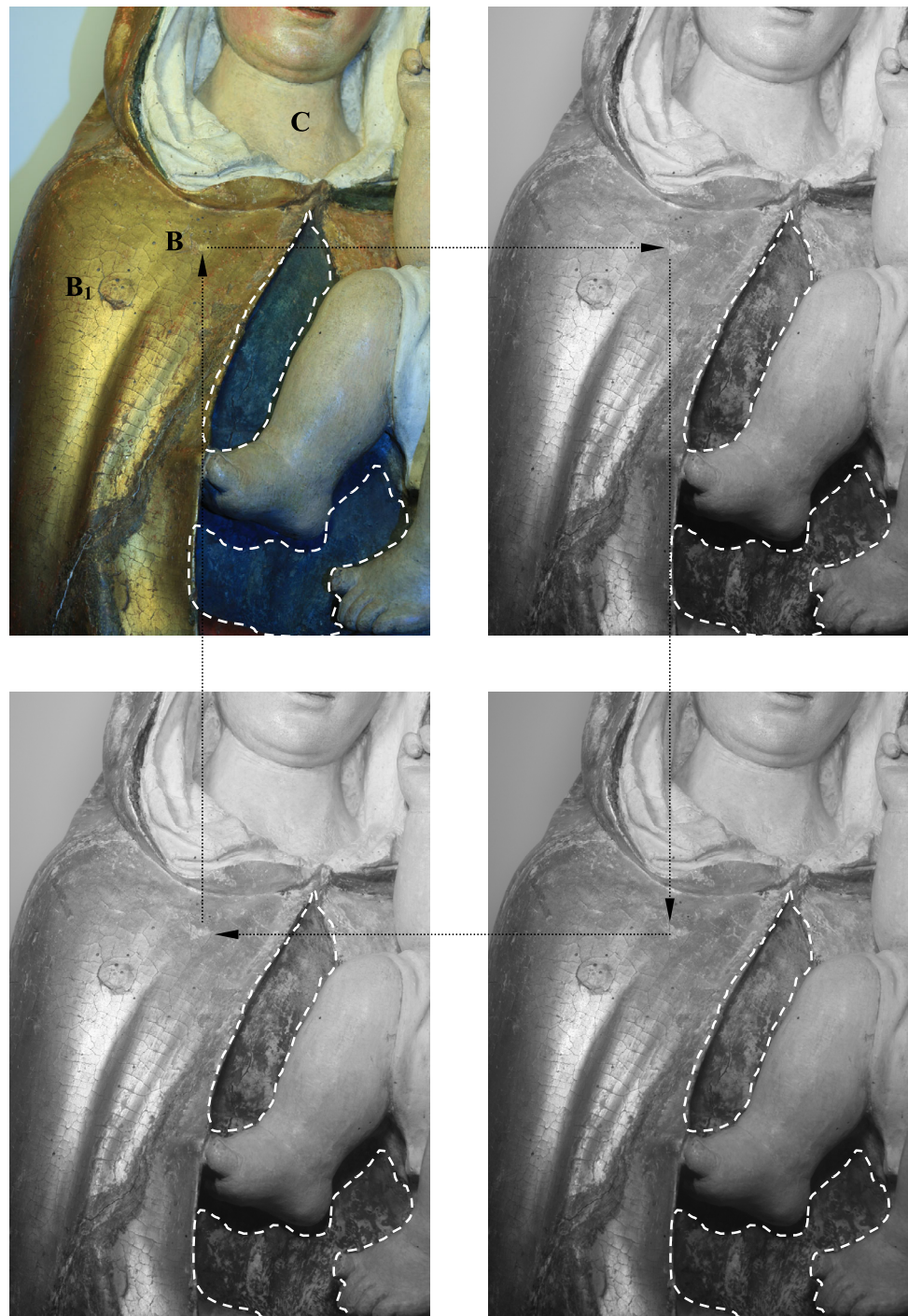
band: 380–1000 nm) and three different filters to limit the spectrum to 715, 850, and 1000 nm, also revealed large retouchings of the blue dress of the Virgin (Figs. 6b–d—irregular dotted lines). On the contrary, crack C was not detected and only a slight indication of the lower edge of the splitting B was highlighted by this method. Splitting B_1, on the other hand, was already evident working with a VIS filter (Fig. 6a) mounted on the camera (dotted arrows).

The NDT measurements corresponding to the area covered by the defects A and A_1 are reported in Fig. 7. Defect A_1 was detected by all methods, i.e., NIR (Fig. 7a), SH (Figs. 7b and 7d), and PPT (Fig. 7c), while two indications of defect A appear in Figs. 7c and 7d. Taking into account the defects' shape, it is possible to say that they might correspond to inclusions of foreign materials, probably two inserts having a structural function. These inserts, highlighted with dotted circles, could be linked to the remodeling of the Child's face over time (Figs. 1a and 1b).

Confirmation of this ancient restoration was provided by the unexpected fringes' configuration (Figs. 7b and 7d) and the differences in colors (from white to dark) after the PPT processing (Fig. 7c), of the nose–mouth–chin zone and of the jowl zone of the Child, respectively.

Following these observations, two micropieces of material were removed from the face of the Child, exactly in correspondence of these two characteristic zones, in order to analyze them by XRF and SEM-EDS techniques. To the naked eye, irregularities are not apparent: the hue of colors looks the same, and no traces of repairs can be identified. The po-sitions of the microsamples are marked by two crosses in Fig. 7c.

The XRF experimental results are shown in Fig. 8. The graph in Fig. 8a is the instrumental background, while Fig. 8b represents the nose result, and finally Fig. 8c the jowl result. The second one contains a large amount of strontium and lead, together with a high probability of chalk and white lead. This is a typical stratigraphy of a painted statue: chalk and glue as preparation and white lead as a primer. On the contrary, the last one has a high quantity of lead and zinc, together with a high probability of white lead and zinc. Although the absence of strontium in the graph reported in Fig. 8c is not significant, since it depends on the sampling (deep or shallow), the traces of zinc are very significant, indicating also the presence of white lead and white zinc (the latter is a pigment widely used in the nineteenth and early twentieth century, and currently employed only sporadically) [57, 59, 60].

The main contributions to noise signal N in XRF spectra come from: (a) the continuum under the peak (N_{cont}), a peak observed in a measurement performed for a blank sample (with a net peak area N_{blank}), a peak observed in the absence of sample (instrumental background, net peak area N_{bkg}), a spectral interference (net peak area N_{SI}). In general, it is a mistake to believe that standard laboratory data are free of errors: standard laboratory data can be "noisy" and are not necessarily an error-free representation of reality. This can be seen when laboratory analyses from two different laboratories are compared to one another in the same way that

Fig. 7 The Virgin with her Child, NIR, HI, and IRT results of the defects A and A_1: (**a**) filter at 850 nm, (**b**) sandwich holography, 1st fringes' configuration, (**c**) PPT phasegram $f = 0.0017$ Hz, and (**d**) sandwich holography, 2nd fringes' configuration
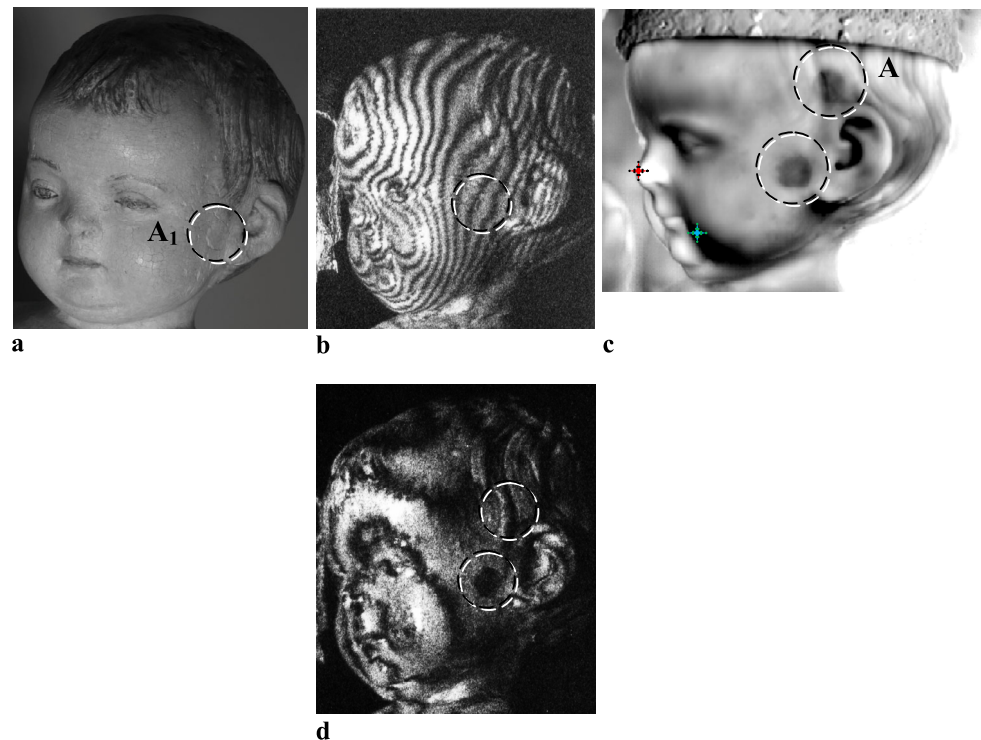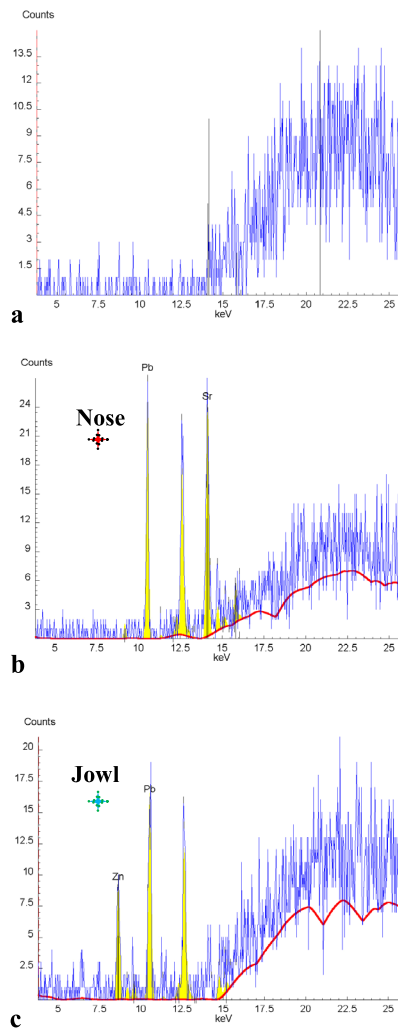
Fig. 8 XRF results: (**a**) instrumental background; (**b**) microsample of the nose, and (**c**) microsample of the jowl

XRF and laboratory data are compared [61]. However, in the XRF measurements here presented, the main parameters that affect the XRF performance, such as measurement time, contaminant concentrations, sample preparation, interference effects, matrix effects, and operator skills were taken into account in order to avoid mistakes in the discussion of the XRF experimental results.

In order to have a sure description of the stratigraphy of the microsamples, stereoscopic images (using a LEICA S8AP0 stereo microscope) (Figs. 9a, b) and images coming from a scanning electron microscopy (SEM) (Philips XL30/CP) were acquired (Figs. 9c, d, e, f) [62, 63]. In particular, Fig. 9a is the stereomicroscopic image inherent the microsample of the nose, while Fig. 9b is the stereomicroscopic image inherent the microsample of the jowl. Seeing these figures, it is already possible to appreciate the difference in the stratigraphy if the two microsamples are compared.

Differences in the consistency of the various layers that form the microsamples can be also appreciated working at WD 200 μm (Figs. 9c, d) during the SEM acquisitions. However, to better understand the structures of the deeper layer, a magnification (WD 50 μm) of the microsample of the nose is reported in Fig. 9e, while a magnification of the microsample of the jowl is shown in Fig. 9f. In practice, the SEM uses a focused beam of high-energy electrons to generate a variety of signals at the surface of solid specimens. The signals that derive from electron-sample interactions reveal information about the sample including external morphology (texture), chemical composition, and crystalline structure, and orientation of materials making up the sample.

Data were collected over selected areas of the surface of the samples, and two-dimensional images that display spatial variations in these properties were generated (Figs. 9c–f). For example, the presence of a microneedles texture can be visualized only in Fig. 9f (jowl) and not in Fig. 9e (nose).

During the SEM acquisitions, a back-scattered electron detector (BSE) was used. In this case, "brighter" BSE intensity is correlated with greater average Z (atomic number) in the sample, while "dark" areas have lower average Z. Before the step named "acquisition of images," the microsamples: (a) were incorporated inside an epoxy resin that cures at room temperature, (b) were polished, (c) were mounted on stubs, and (d) were covered with a thin layer of gold using the sputtering method (Balzers Union—SCD040).

An Energy-Dispersive x-ray Spectroscopy (EDS) system (OXFORD—INCA x-act) integrates the SEM instrument. The EDS detector contains a crystal that absorbs the energy of incoming x-rays by ionization, yielding free electrons in the crystal that become conductive and produce an electrical charge bias. The x-ray absorption thus converts the energy of individual x-rays into electrical voltage of proportional size; the electrical pulses correspond to the characteristic x-rays of the element [63].

In order to integrate the SEM results shown in Figs. 9e, f, i.e., to qualitatively characterize the chemical elements of the deeper parts of the microsamples (lower layers), it is possible to observe two spectrums (Figs. 9g, h) linked to the small selected areas marked by fuchsia rectangles. The microsample inherent to the nose shows an important amount of the following chemical elements: carbon, oxygen, magnesium, phosphorus, sulfur, potassium, and calcium; while the microsample inherent to the jowl shows the presence of: carbon, oxygen, sulfur, chlorine, and calcium. These results are correlated to the difference in the texture shown in Figs. 9e, f.

In this way: (a) the SEM and XRF results are supported by a chemical-physical method that confirms the innovative integrated approach described herein, and (b) the terms "non or microdestructive techniques" used in this work are well suited in our case.

Fig. 9 (**a**) Stereomicroscopic image inherent the micro-sample of the nose, (**b**) stereomicroscopic image inherent the micro-sample of the jowl, (**c**) SEM image of a part of the micro-sample of the nose, (**d**) SEM image of a part of the micro-sample of the jowl, (**e**) SEM image (magnification) of the deeper part of the micro-sample of the nose, (**f**) SEM image (magnification) of the deeper part of the micro-sample of the jowl, (**g**) EDS spectrum inherent the microsample of the nose, and (**h**) EDS spectrum inherent the micro-sample of the jowl
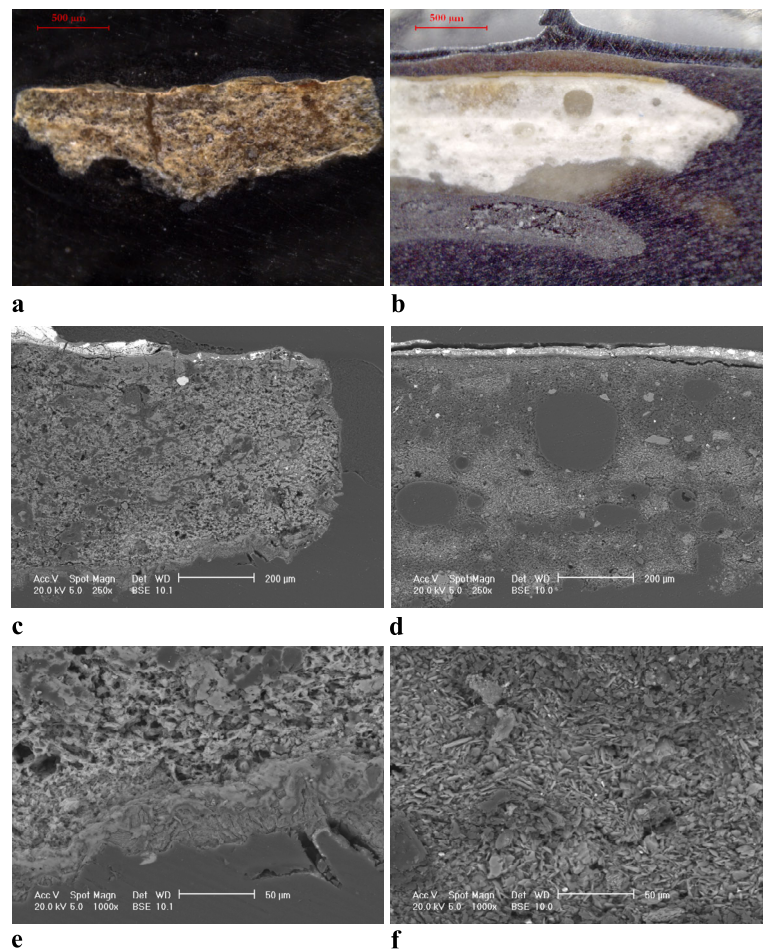
Some HI experimental results obtained by SH and holographic contouring techniques are shown in Figs. 10a and 10b. The golden mantle was heated by a flow of moderately warm air and the surface temperature rose three degrees (°C) in respect to the ambient temperature [9, 10, 64]. In fact, due to the sensitivity to surface deformations, the technique can be used to gain meaningful information with regards to the structural characteristics of an artwork, by observing the surface movements produced when it is subjected to a mild stressing force. As such, it offers the potential for inspection problems where the defect of interest can be made manifest as an anomaly in an otherwise regular interferometric fringe pattern; the stressing technique must be devised is such a way that the anomalies induce detectable perturbations in the surface deformation [26, 38]. However, the temperature rise was maintained below the fluctuations of the ambient temperature ($\Delta T = 6.1$ °C, see Table 1). In this case, the Virgin with her Child statue was absolutely not damaged by the heat flow applied [65].

In particular, Fig. 10b shows the application of the holographic contouring method to the diagnosis of defect B, as well as a 3D plot coming from the wavelet transform analysis. Both results are reported as appendages in Fig. 10b. It

has been possible to pinpoint the detached area and quantify the volume: ≈ 84 mm^3 [9].

In order to establish the difference between an inclusion of foreign material (defects A and A_1) and a splitting (defects B and B_1), the different thermal imprints processed by the same technique, i.e., PPT (Figs. 7c and 10c), can be compared. In Fig. 10c, the detached areas correspond to the bright spots, which surround the central darker zones, while in Fig. 7c, the inclusions appear as dark spots. Although the heating time for defects A and A_1 was twice the one for defects B and B_1 (see Table 1), the phasegram presented in Fig. 7c correspond to a lower frequency than the frequency of the phasegram in Fig. 10c.

It is possible to demonstrate, following the criterion established by the authors in [13] that the detection of the planar coordinates of the B defect (size of the defect), it is possible if the higher-order statistic thermography (HOST) technique (Kurtogram result) with various methods linked to the watershed segmentation concept are combined into a script written in Matlab$^©$ environment [56, 66–68]. A detailed discussion of the images coming from this method and inherent the present case will be published in the future. The measurement conditions of the IRT set-up were
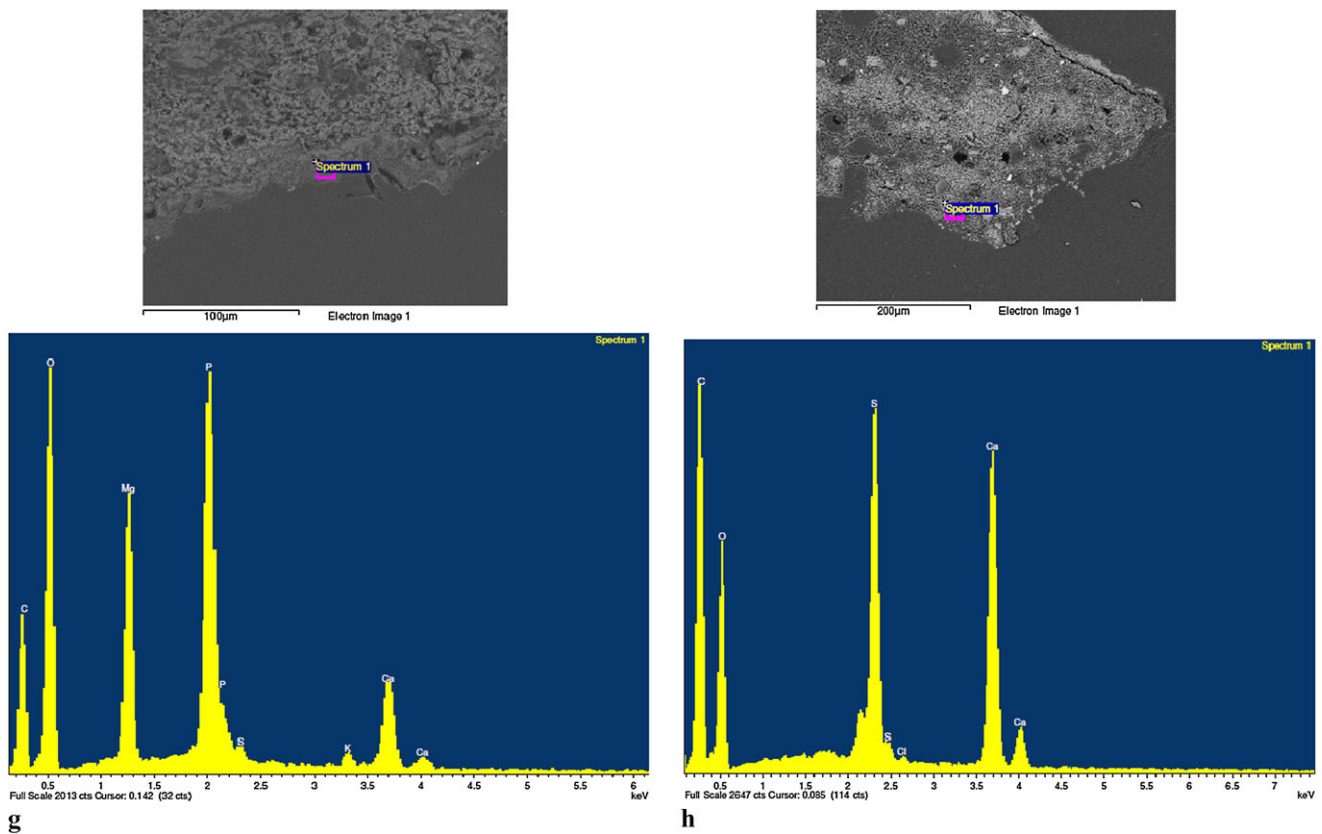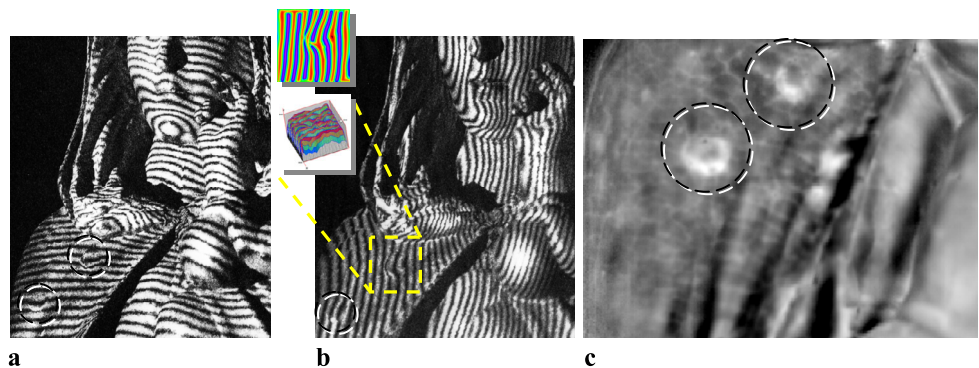
Fig. 9 (*Continued*)

Fig. 10 The Virgin with her Child, HI, and IRT results of the defects B and B_1: (**a**) sandwich hologram, (**b**) holographic contouring and processing of the defect B, and (**c**) PPT phasegram $f = 0.0026$ Hz

applied in order to perform the HOST/Segmentation method are reported in Table 1 also to demonstrate that the ambient temperature where the statue was preserved it was very variable, i.e., the work of art was not preserved inside a museum having the environmental conditions (T_{amb} °C, U.R. %) automatically controlled.

However, in order to complete the discussion here presented, it is necessary to say that, knowing the field of view of the thermo-camera (0.35×0.26 at 1 m), as well as the perpendicular distance between the lens and the defect B, the damaged area can be estimated: ≈ 280 mm^2. Integrating the optical and thermographic results was possible to

retrieve the third dimension of the defect, i.e., the height respect to the painted plane: ≈ 0.3 mm. The latter dimension was confirmed using a digital indicator: 0.331 mm.

During the inspection of the face of the Virgin, the NIR approach was not useful to reveal the presence of any defect (Fig. 11a), although the SH technique clearly detected a vertical crack on the forehead (defect D—Fig. 11b). Manipulating the fringes pattern, a configuration very close to that of the Child's face (Fig. 7b) appears in Fig. 11d. Again, comparing Figs. 1a and 1b, it is possible to infer that the face of the Virgin was deeply restored over the time as well. The good match, highlighted with four dotted arrows, be-
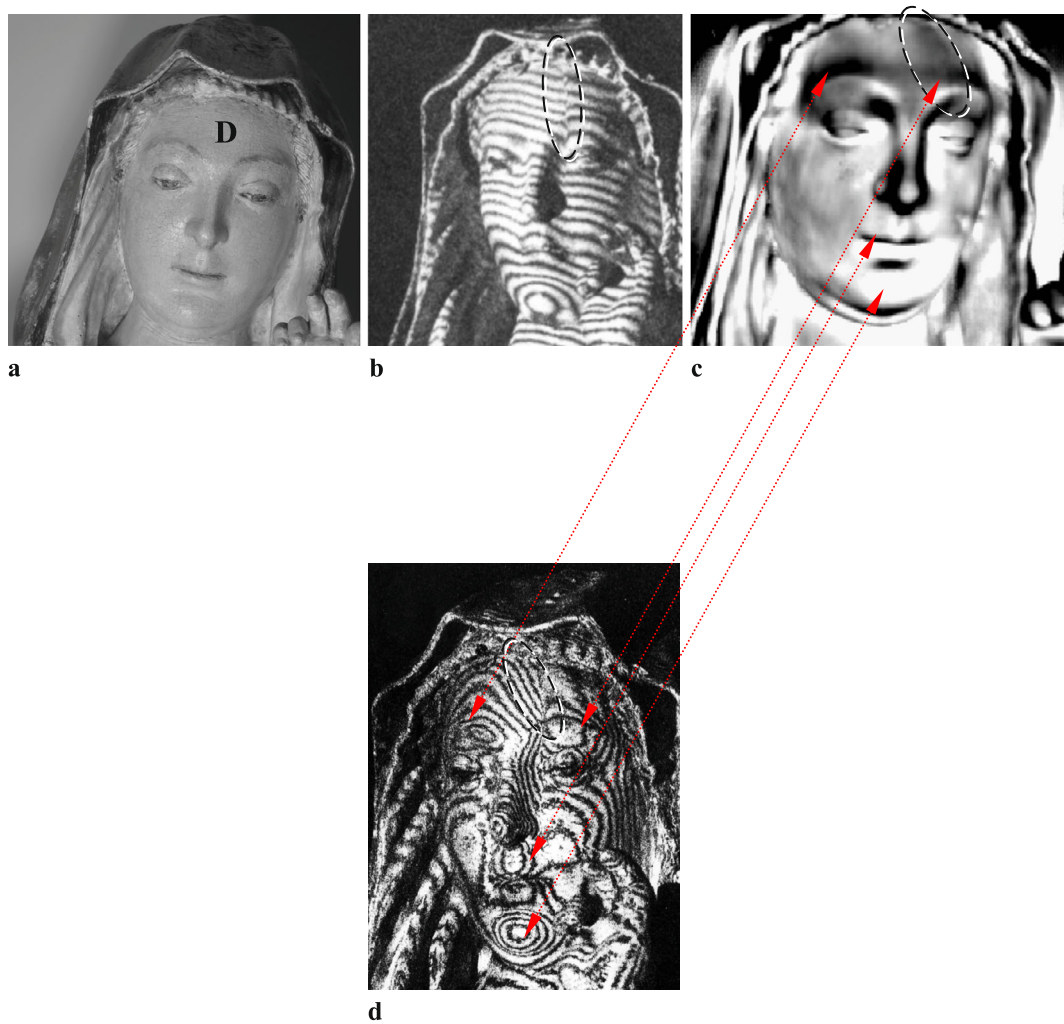
Fig. 11 The Virgin with her Child, NIR, HI, and IRT results of the defect D: (**a**) filter at 850 nm, (**b**) sandwich holography—1st fringes configuration, (**c**) PPT phasegram $f = 0.0026$ Hz, and (**d**) sandwich holography—2nd fringes configuration
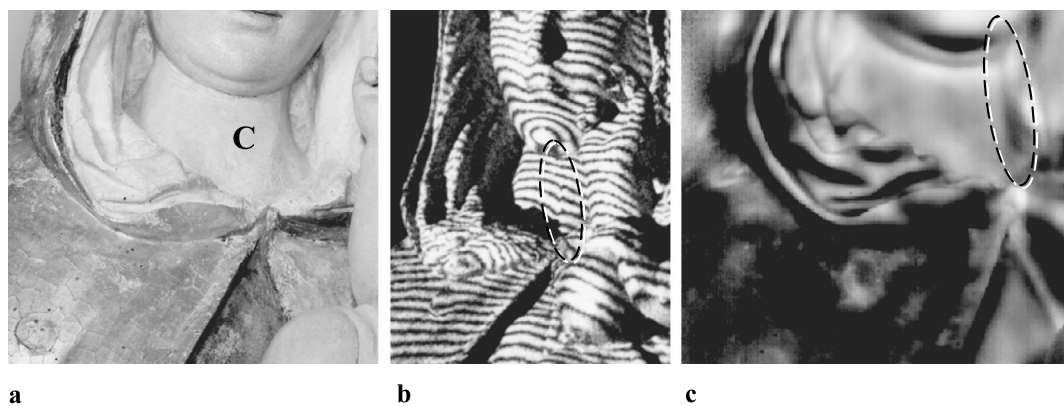

Fig. 12 The Virgin with her Child, NIR, HI, and IRT results of the defect C: (**a**) filter at 850 nm, (**b**) sandwich holography, and (**c**) PPT phasegram $f = 0.0026$ Hz

tween the fringes configuration (Fig. 11d) and the dark or bright spots in the PPT phasegrams in the areas around the eyebrows, maxilla, and chin (Fig. 11c), confirms the valid-ity of the proposed method without performing further XRF and/or SEM-EDS analysis. In this case, the thermo-camera was installed in front of the Virgin's face and not in a lat-

eral position as was the case during the inspection of the Child' face (Fig. 7c). This is a fundamental consideration, which eliminated any doubts about the relationship between the complex surface geometry inspected, as well as its orientation, and the PPT results.

The inspection of the Virgin's neck was a convenient choice because a continuation of the crack D was detected both by SH and PPT (defect C in Figs. 12b and 12c). Also in this case, the crack was not revealed by NIR reflectography. Keeping in mind the location of cracks C and D, it is reasonable to suppose that they are the same crack at two different locations, which is not detectable in the through the face because it is deeper. In addition, the wooden support of the statue is a single piece of cedar wood, and cracks propagation inside this natural composite material is well known [69, 70].

5 Conclusion

Diagnostics of painted materials without any accompanying microstructural characterization are the interest of many research groups [71–73]. Technically speaking, in order to characterize a component, at least a form of microscopy (light, electron, acoustic) or analysis (microanalysis and surface analytical techniques) is needed.

In the present case, the XRF technique combined with the SEM-EDS technique, support the deductions coming from an integrated approach between optical (SH), nonthermal (NIR), and thermographic (SPT) NDT techniques. The combination of methods and/or the data processing used, can be considered as innovative, above all if applied to a polychromatic painted wood. Currently, the approach is joined to a historical-technical research, which improves the results and allows to differentiate between different types of defects (cracks, detached areas, and inclusions of foreign materials), taking into account the experimental results. This work has also underlined that the NIR reflectography approach, in some cases, is not adequate to establish if an artistic object has been restored in the past, as well as it shows an intelligent combined method between the holographic contouring, HOST, and the image segmentation algorithms, in order to determine the volume and the planar extension of a splitting inherent to the golden mantle of the Virgin (defect B).

In addition, the emboss effect "enhances" the main part of the Virgin with her Child statue relative to its background. This filter contrast lines of the image and adds shadows to them to imitate "depressed" areas; more brighter is the area, and more "depressed" it will appear. For this, it was very useful to detect the *craquelure* areas caused by the age.

At this point, it is possible to affirm that this work can be appreciated as a reference for the restorers involved in the conservation of wooden structures covered by layers of painting, since the proposed joint approach also permits to establish a historical reconstruction of the restorations.

Finally, an interesting perspective of the work will be to compare data collected by using SH and holographic contouring techniques (localizations of inclusions and defect sizes) with the scientific examinations usually used in the cultural heritage field, i.e., X-ray radiography and tomography [74]. The integration to the present study will be realized in a future publication, working with another international group that is an expert and that has the necessary equipment in these fields of research.

References

1. Bulletin of the metropolitan Museum of Art, A German statue of the thirteenth century, http://www.metmuseum.org/pubs/bulletins/1/pdf/3255622.pdf.bannered.pdf. Accessed on 20 June 2013
2. B.D. Fahlman, *Materials Chemistry*, 2nd edn. (Springer, New York, 2011), pp. 1–747
3. C. Ibarra-Castanedo, S. Sfarra, D. Ambrosini, D. Paoletti, A. Bendada, X. Maldague, QIRT J. **5**, 1768–6733 (2008)
4. H. Rottenkolber, W. Juptner, Holographic interferometry in the next decade, in *Laser Interferometry: Quantitative Analysis of Interferograms*, ed. by R.J. Pryputniewicz. Proc. SPIE, vol. 1162, 3rd edn. (SPIE, San Diego, 1989), pp. 2–15
5. K. Şerifaki, H. Böke, Ş. Yalçin, B. Ipekoğlu, Mater. Charact. **60**, 303–311 (2009)
6. M. Brunetti, E.L. De Capua, N. Macchioni, S. Monachello, Ann. Sci. For. **58**, 607–613 (2001)
7. J.R.J. van Asperen de Boer, Stud. Conserv. **11**, 45–46 (1966)
8. R.W. Arndt, Infrared Phys. Technol. **53**, 246–253 (2010)
9. P. Carelli, D. Paoletti, G. Schirripa Spagnolo, A. D'Altorio, Opt. Eng. **30**, 1294–1298 (1991)
10. S. Amadesi, A. D'Altorio, D. Paoletti, Appl. Opt. **21**, 1889–1890 (1982)
11. N. Carmona, I. Ortega-Feliu, B. Gómez-Tubío, M.A. Villegas, Mater. Charact. **61**, 257–267 (2010)
12. J.F. Asmus, Mater. Charact. **29**, 119–128 (1992)
13. S. Sfarra, C. Ibarra-Castanedo, F. Lambiase, D. Paoletti, A. Di Ilio, X. Maldague, Meas. Sci. Technol. **23**, 115601 (2012)
14. Encyclopaedia Britannica, www.britannica.com/EBchecked/topic/101070/cedar. Accessed on 02 January 2013
15. S. Montorio, *Lo Zodiaco di Maria, Zodiaco di Maria, ovvero Le dodici province del Regno di Napoli, come tanti segni, illustrate da questo sole per mezzo delle sue prodigiosissime immagini, che in esse quasi tante stelle risplendono* (Carbonara, Naples, 1715), pp. 1–606
16. C. Brandi, *Teoria del restauro* (Einaudi, Turin, 1977), pp. 1–154
17. J.C. Rich, *Sculpture in Wood* (Dover, New York, 1992), pp. 1–175
18. C.C. Carstenson, *The Craft and Creation of Wood Sculpture* (Dover, New York, 1981), pp. 1–180
19. S. Bordini, *Materia e immagine—Fonti sulle tecniche della pittura* (Leonardo & De Luca Eds., Rome, 1991), pp. 1–269

20. E. Antonucci, *Roio e il suo Santuario* (Eco Ed., Teramo, 1986), pp. 1–117

21. F. Murri, *Roio e il suo Santuario* (La Fonte Ed, Pescara, 1989), pp. 1–159

22. A. Signorini, *La Diocesi di Aquila descritta ed illustrata—Vol. 1* (Stabilimento Tipografico Grossi, L'Aquila, 1868), pp. 1–101

23. G. Manuelli, Prima visita pastorale 1931–1934 (L'Aquila, 1934), pp. 1–37

24. M. Paglia, A. Trionfi, *S. Maria della Croce in Roio—Poemetto storico religioso in ottava rima* (Officine Grafiche Vecchioni, L'Aquila, 1929), pp. 1–61

25. O. Luciani, Madonne in mostra al Castello Piccolomini di Celano (L'Aquila), http://www.oresteluciani.eu/Madonne%20in%20mostra%20al%20Castello%20Piccolomini%20di%20Celano.pdf. Accessed on 03 January 2013

26. C.M. Vest, *Holographic Interferometry* (Wiley, New York, 1979), pp. 1–480

27. J.J. Zelenka, J.R. Varner, Appl. Opt. **7**, 2107–2110 (1968)

28. K.J. Gasvik, K.J. Svik, *Optical Metrology* (Wiley, London, 2003), pp. 1–374

29. P. Demattia, V. Fossati-Bellani, Opt. Commun. **26**, 17–21 (1978)

30. C.A. Sciammarella, Opt. Eng. **21**, 447–457 (1982)

31. N. Abramson, *The Making and Evaluation of Holograms* (Academic Press, London, 1982), pp. 1–326

32. L. Meitner, Z. Phys. **9**, 131–144 (1922)

33. M.C. Miller, X-Ray Fluorescence, www.fas.org/sgp/othergov/doe/lanl/lib-www/la-pubs/00326405.pdf. Accessed on 01 December 2012

34. M. Mantler, M. Schreiner, X-Ray Spectrom. **29**, 3–17 (2000)

35. R. Cesareo, A. Brunetti, S. Ridolfi, X-Ray Spectrom. **37**, 309–316 (2008)

36. R. Jenkins, *X-ray Fluorescence Spectrometry*, 2nd edn. (Wiley, New York, 1999), pp. 1–207

37. R. Jenkins, R.W. Gould, D. Gedcke, *Quantitative X-ray Spectrometry* (Dekker, New York, 1981), pp. 1–586

38. S. Sfarra, P. Theodorakeas, C. Ibarra-Castanedo, N.P. Avdelidis, A. Paoletti, D. Paoletti, K. Hrissagis, A. Bendada, M. Koui, X. Maldague, Insight **54**, 21–27 (2012)

39. R.B. Dinwiddie, S.W. Dean, Case study of IR reflectivity to detect and document the underdrawing of a 19th century oil painting, in *Thermosense XVIII*. Proceedings SPIE, vol. 6205, Florida (2006)

40. C. Daffara, E. Pampaloni, L. Pezzati, M. Barucci, R. Fontana, Acc. Chem. Res. **43**, 1–15 (2010)

41. E. Walmsley, C. Metzger, J.K. Delaney, C. Fletcher, Stud. Conserv. **39**, 217–231 (1994)

42. J.R.J. van Asperen, Stud. Conserv. **14**, 96–118 (1969)

43. G. Wecksung, R. Evans, J. Walker, M. Ainsworth, J. Brealey, G.W. Carriveau, Assembly of infra-red reflectograms by digital processing using a portable data collecting system, in *ICOM Committee for Conservation, 8th Triennial Meeting*, Sydney (1987)

44. J.K. Delaney, Examination of the visibility of underdrawing lines as a function of wavelength, in *ICOM Committee for Conservation, 10th Triennial Meeting*, Washington (1993)

45. D. Bertani, M. Cetica, P. Poggi, G. Puggioni, E. Buzzegoli, D. Kunzelman, S. Cecchi, Stud. Conserv. **35**, 113–116 (1990)

46. J. Coddington, The use of infra-red vidicon and image digitizing software in examining 20th century works of art. AIC Paintings Specialty Group Postprints. Albuquerque (1991)

47. R.W. Astheimer, *Handbook of Infrared Radiation Measurement* (Barnes Engineering Company, Stamford, 1983), pp. 1–113

48. C. Weiner, Improved acquisition of underdrawings in oil-paintings using IR-Reflectography. Final Report SIMG-503. Rochester: Rochester Institute of Technology (1998)

49. X.P.V. Maldague, *Theory and Practice of Infrared Technology for Non-destructive Testing* (Wiley, New York, 1991), pp. 1–704

50. D.L. Balageas, J.C. Krapez, P. Cielo, J. Appl. Phys. **59**, 348–457 (1986)

51. V. Vavilov, T. Kauppinen, E. Grinzato, Res. Nondestruct. Eval. **9**, 181–200 (1997)

52. Basic signal processing, Chap. 9, www.cs.princeton.edu/courses/archive/fall00/cs426/papers/hanrahan95.pdf. Accessed on 04 July 2012

53. X.P.V. Maldague, S. Marinetti, J. Appl. Phys. **79**, 2694–2698 (1996)

54. C. Ibarra-Castanedo, X. Maldague, QIRT J. **1**, 47–70 (2004)

55. F.J. Madruga, C. Ibarra-Castanedo, O.M. Conde, J.M. López-Higuera, X. Maldague, Nondestruct. Test. Eval. Int. **43**, 661–666 (2010)

56. A. Chanda, D.D. Majumder, *Digital Image Processing and Analysis*, 2nd edn. (PHI Learning Pvt., Ltd, New Delhi, 2011), pp. 1–471

57. R. Mayer, *The Artist's Handbook of Materials and Techniques*, 5th edn. (Viking Adult, New York, 1991), pp. 1–784

58. F. Brunello, *Cennini Cennino: Il libro dell'arte* (Neri Pozza, Vicenza, 1993), pp. 1–207

59. G. Piva, *L'arte del restauro—Il restauro dei dipinti nel sistema antico e moderno*, 3rd edn. (Hoepli, Milano, 1988), pp. 1–442

60. L. Bux, G. Morabito, F. Prosperetti, F. De Chirico, P. Martino, S. De Fiores et al., *La Madonna dei poveri di Seminara—Il culto, la storia dell'arte, il restauro* (Rubbettino, Soveria Mannelli, 2011), pp. 1–225

61. Module 2: Basic XRF concepts, http://www.clu-in.org/conf/tio/xrf_080408/prez/XRF_02pdf.pdf. Accessed on 23 June 2013

62. A. Giumlia-Mair, C. Albertson, G. Boschian, G. Giachi, P. Iacomussi, P. Pallecchi, G. Rossi, A.N. Shugar, S. Stock, Mater. Technol. **25**(5), 245–261 (2010)

63. H. Kahn, E.S. Mano, M.M.M.L. Tassinari, J. Miner. Mater. Charact. Eng. **1**(1), 1–9 (2002)

64. H.J. Tiziani, Opt. Quantum Electron. **21**, 253–282 (1989)

65. S. Sfarra, C. Ibarra-Castanedo, D. Paoletti, X. Maldague, Mater. Eval. **5**, 561–570 (2013)

66. R.C. Gonzalez, R.E. Woods, *Digital Image Processing*, 2nd edn. (Prentice Hall, Reading, 2008), pp. 1–954

67. J.C. Russ, *The Image Processing Handbook*, 6th edn. (CRC Press, Boca Raton, 2007), pp. 1–885

68. H. Zhou, J. Wu, J. Zhang, *Digital Image Processing: Part II* (eBook Publishing, Bookboon, 2010), pp. 1–91

69. C. Ibarra-Castanedo, S. Sfarra, D. Ambrosini, D. Paoletti, A. Bendada, X. Maldague, QIRT J. **7**, 85–114 (2010)

70. I. Smith, S. Vasic, Mech. Mater. **35**, 803–815 (2003)

71. C. Daffara, D. Ambrosini, L. Pezzati, D. Paoletti, Opt. Express **20**, 14746–14753 (2012)

72. C.H. Chen, *Ultrasonic and Advanced Methods for Nondestructive Testing and Material Characterization* (World Scientific Publishing, Singapore, 2007), pp. 1–665

73. R.E. Green Jr., Int. Appl. Mech. **38**, 253–259 (2002)

74. F. Casali, Archeom. Műh. **3**(1), 24–28 (2006)